PCCP

PAPER

View Article Online
View Journal | View Issue

Cite this: *Phys. Chem. Chem. Phys.*, 2025, **27**, 15594

Low lattice thermal conductivity induced by rattling-like vibration in RbCaX (X = As, Sb) compounds with excellent thermoelectric properties†

Jingyi Zhang, ‡[a] Junhao Peng, ‡[a] Runqing Zhang, [a] Yanwei Liang,[a] Zihan Xu,[a] Renhai Wang, [a] Fugen Wu,*[b] Da Wan,[c] Pengfei Zhang,[c] Shulin Bai[c] and Huafeng Dong*[a]

Layered alkali metal (A)–alkaline earth metal (AE)–pnictogen (Pn = N, P, As, Sb, and Bi) compounds are promising candidates for thermoelectric applications due to their thermal stability and low thermal conductivity. This study systematically investigates and compares the anisotropic thermoelectric properties of the layered RbCaAs and RbCaSb compounds using density functional theory (DFT) and semiclassical Boltzmann transport theory. The results show that the rattling thermal damping effect from weak Rb–As/Sb bonds in RbCaX (X = As, Sb) compounds leads to low lattice thermal conductivity (~3.22/1.20 and ~1.90/0.94 W m^{-1} K^{-1} at 300 K along the *x*-/*y*-direction). The n-type RbCaSb exhibits significantly optimal dimensionless thermoelectric figure of merit (*ZT*) of ~3.19 (cross-plane) and ~1.71 (in-plane) at 900 K, which are significantly higher than ~0.54 and ~0.80 of n-type RbCaAs and typical layered thermoelectric materials like p-type SnSe (*ZT* ~2.6, 923 K) and BiCuOSe (predicted *ZT* ~0.75, 900 K). This enhancement is attributed to the lower scattering rate boosting power factor, and lattice softening induced by the heavy Sb elements strengthens anharmonic phonon scattering and reduces lattice thermal conductivity. These findings highlight RbCaSb as a promising candidate in the field of thermoelectric materials.

Received 27th April 2025,
Accepted 3rd July 2025

DOI: 10.1039/d5cp01602a

rsc.li/pccp

1 Introduction

Thermoelectric (TE) materials enable direct thermal-to-electrical energy conversion, providing a critical solution to the global energy crisis.[1,2] Their development is instrumental in alleviating environmental degradation from carbon-based energy consumption.[3,4] Nonetheless, the widespread application of thermoelectric materials is impeded by their suboptimal energy conversion efficiency, typically quantified by the dimensionless figure of merit *ZT*, defined as $ZT = S^2\sigma T/(K_e + K_l)$, where S, σ, $K_e + K_l$ (K) and T represent the Seebeck coefficient, electrical conductivity, thermal conductivity and absolute temperature, respectively.[5] The inherent conflict between thermal and electrical transport poses a considerable challenge to improving overall *ZT*. Ideal thermoelectric materials require a delicate balance of high electrical conductivity, large Seebeck coefficients, and low thermal conductivity, rendering the pursuit of materials endowed with "phonon glass-electron crystal" (PGEC) attributes a paramount strategy for thermoelectric performance optimization.[6] Notably, low lattice thermal conductivity (K_l) is frequently correlated with pronounced phonon anharmonicity, primarily induced by weak bonding and atomic rattling behavior[7]. Numerous layered materials manifest low K_l and anisotropic thermoelectric transport properties due to the disparity between strong intralayer and weak interlayer interactions.[8–14] The exploration of high-performance thermoelectric materials should focus on strong anharmonicity,[15–17] weak atomic bonding,[18] and intrinsic vacancies.[19] Additionally, the traditional methods for optimizing thermoelectric performance include reducing k_l *via* anharmonic effects[20–22] and nanostructuring,[23,24] as well as improving σ using band engineering.[25,26]

Since the discovery of layered NaMgX (X = P, Sb, As) compounds with exceptional thermoelectric properties,[27] alkali

[a] *Guangdong Provincial Key Laboratory of Sensing Physics and System Integration Applications, School of Physics and Optoelectronic Engineering, Guangdong University of Technology, Guangzhou 510006, China. E-mail: hfdong@gdut.edu.cn*
[b] *The College of Information Engineering, Guangzhou Vocational University of Science and Technology, Guangzhou 510550, China. E-mail: wufugen@gkd.edu.cn*
[c] *College of Materials Science and Engineering, Liaoning Technical University, Fuxin, Liaoning 123000, China*

† Electronic supplementary information (ESI) available. See DOI: https://doi.org/10.1039/d5cp01602a

‡ Equal contribution.

metal (A)–alkaline earth metal (AE)–pnictogen (Pn = N, P, As, Sb, and Bi) have emerged as a focal point in thermoelectric research due to their unique chemical bonding hierarchy, diverse crystal structures, and chemical tunability. The materials typically exhibit a stoichiometric composition of A–AE–Pn (1 : 1 : 1) and crystallize in various structural types, such as cubic Half–Heusler (*e.g.*, LiMP),[28] cubic LiGeGe (*e.g.*, LiBeSb),[29] hexagonal ZrBeSi (*e.g.*, NaBeSb),[30] or cubic PbFCl (*e.g.*, NaMgAs).[31] Early studies primarily focused on light alkali metal (*e.g.*, Li, Na, K) systems, for instance, Half–Heusler compounds like LiSrX (X = N, P and As) exhibited promising electrical and thermal transport properties, with high power factors observed under p-type regions.[32] Subsequently, NaAESb (AE = Ca, Sr, Ba) compounds achieved *ZT* values of ∼1 at 500 K, driven by stronger phonon–phonon interactions at higher temperatures, effectively reducing thermal transport properties.[33] Furthermore, the KAEPn family (AE = Mg, Ca; Pn = Sb, Bi) has been extensively studied for its pressure-induced low lattice thermal conductivity and optimized thermoelectric performance through alloy engineering.[34–38]

Despite the excellent electronic properties of light alkali metal-based A–AE–Pn compounds, their limited structural stability at evaluated temperatures restricts practical applications. Consequently, research endeavors have pivoted towards heavy alkali metals (*e.g.*, Rb, Cs)- and heavy pnictogens (*e.g.*, Sb, Bi)-based A–AE–Pn compounds, which often exhibit stronger phonon anharmonicity and lower lattice thermal conductivity, offering new thermoelectric optimization. Recently, Zhang *et al.* screened 488 compounds through thermodynamic analysis and identified 20 thermodynamically stable Half–Heusler compounds, RbYZ (Y = Be, Mg, Ca, Sr, Ba; Z = P, As, Sb, Bi), systematically investigating their electronic, optical, and thermoelectric properties.[39,40] This has accelerated research into Rb-based A–AE–Pn compounds with diverse phase structures. Among these compounds, PbFCl-type RbCaAs and RbCaSb have garnered attention for their high electrical conductivity and significant power factors.[41,42] However, existing studies have insufficiently addressed phonon and multi-carrier scattering mechanisms in layered RbCaAs and RbCaSb compounds, and the origins of low lattice thermal conductivity and strategies for optimizing electrical transport remain unclear, requiring further investigation.

To elucidate these issues, this study employs first-principles calculations and Boltzmann transport theory to systematically investigate the thermoelectric properties of layered RbCaX (X = As, Sb) compounds. By analyzing the effects of acoustic deformation potential (ADP) scattering, ionized impurity (IMP) scattering, and polar optical phonon (POP) scattering on carrier mobility and relaxation time, we find that n-type RbCaSb exhibits remarkable anisotropic *ZT* values of ∼3.19 (cross-plane) and ∼1.71 (in-plane) at 900 K, significantly surpassing n-type RbCaAs (∼0.80 and ∼0.54). The rattling-like scattering behavior in the RbCaX (X = As, Sb) compounds is identified as a pivotal factor contributing to low lattice thermal conductivity, supported by in-depth analysis of temperature-dependent atomic displacement parameter (ADP). The results highlight the potential of RbCaSb as a high-performance thermoelectric material and provide important theoretical insights for the design and application of layered A–AE–Pn compounds.

2 Computational details

2.1 Density functional theory calculations

All the density functional theory (DFT) calculations were performed within the framework of the Vienna ab initio simulation package (VASP),[43] employing generalized gradient approximation (GGA) in conjunction with the projector-augmented wave (PAW) method.[44,45] The exchange–correlation potential was modelled using the Perdew, Burke, and Ernzerhof parametrized generalized gradient approximation (GGA-PBE).[46] The plane wave cutoff energy was increased to 600 eV during structure relaxation to avoid Pulay stress. A 6 × 6 × 4 Monkhorst–Pack *k*-point mesh in the irreducible Brillouin zone and energy and force convergence criteria to 10^{-8} eV and 10^{-5} eV Å^{-1} were applied for structure relaxation. Furthermore, considering the self-interaction errors in the GGA–PBE framework tend to underestimate the fundamental energy band gaps,[47,48] the range-separated hybrid functional proposed by Hey, Scuseria, and Ernzerhof (HSE06) was adopted to enhance the description of electronic properties and structural parameters.[49,50] To accurately describe the weak interlayer interactions, the D3 correction method was incorporated to account for van der Waals dispersion forces.[51,52]

The chemical stability convex hull of RbCaX (X = As, Sb) was constructed by collecting possible binary phases in the Rb–Ca–X chemical space from the Materials Project database,[53] performing PBE relaxation and static self-consistency calculations on these binary phases and ternary RbCaX (X = As, Sb), and plotting the diagrams using the python-ternary module based on the calculated energy results.

2.2 Electronic transport calculations

The electronic transport properties were calculated using the *ab initio* scattering and transport program (AMSET) package.[54] Solving the Boltzmann transport equation *via* the constant relaxation time approximation (CRTA) usually overestimates the *ZT*.[54,55] In contrast, AMSET improves accuracy by employing the momentum relaxation time approximation (MRTA), explicitly calculating the scattering rates of electronic states within the Born approximation. AMSET accounts for four scattering mechanisms: polar optical phonon (POP), acoustic deformation potential (ADP), ionic impurity (IMP), and piezoelectric (PIE) scattering. These scattering mechanisms are incorporated into *ZT* calculations *via* electrical conductivity (σ) and electronic thermal conductivity (K_e). For RbCaX (X = As, Sb), the piezoelectric constants were calculated to be 0, and thus PIE scattering was excluded. The Seebeck coefficients were also calculated by AMSET software but are unaffected by scattering mechanisms.

The AMSET software was employed to calculate the electronic scattering rates as described by the Fermi golden rule, and

the elastic scattering rates from a state nk to $mk + q$ can be written:[54]

$$\tau_{nk\to mk+q}^{-1} = \frac{2\pi}{\hbar}|g_{nm}(k,q)|^2\delta(\varepsilon_{nk} - \varepsilon_{mk+q}) \quad (1)$$

and a corresponding equation was presented for the inelastic scattering rate:

$$\tau_{nk\to mk+q}^{-1} = \frac{2\pi}{\hbar}|g_{nm}(k,q)|^2\times\left[\left(n_q + 1 - f^0_{mk+q}\right)\delta\left(\Delta\varepsilon^{nm}_{k,q} - \hbar\omega_q\right) + \left(n_q + f^0_{mk+q}\right)\delta\left(\Delta\varepsilon^{nm}_{k,q} + \hbar\omega_q\right)\right] \quad (2)$$

where $\hbar$ denotes the reduced Planck constant, δ represents the Dirac delta function, ε_{nk} signifies the energy of the $|nk|$ state, n characterizes the Bose–Einstein distribution, f pertains to the Fermi–Dirac distribution, and the expressions $-\hbar\omega_q$ and $\hbar\omega_q$ are indicative of phonon emission and absorption processes, respectively. The coefficient $g_{nm}(k,q)$ stands for the coupling matrix element inherent to the analyzed scattering mechanism, while comprehensive formulations of all scattering matrix elements can be found in the referenced source.

Additionally, the band structure, wavefunction coefficients, elastic constants, deformation potentials, static and high-frequency dielectric constants, and polar optical phonon frequencies were computed by DFT and finite difference (FD) methods,[56] which were used as the AMSET input parameters for the determination of carrier relaxation times. The above data are shown in Table S3 (ESI†). Convergence tests for electrical transport parameters are presented in the ESI,† Fig. S4–S7.

2.3 Phonon thermal transport calculations

Phonon dispersions of RbCaX (X = As, Sb) were computed using the Phonopy code[57] and the VASP package based on the second-order interatomic force constants (IFCs) derived from the finite-difference (FD) method. The second-order IFCs were evaluated using a 3 × 3 × 3 supercell (162 atoms) and a 3 × 3 × 3 Monkhorst–Pack q-point mesh. Convergence tests of the phonon dispersion are shown in Fig. S10 and S11 (ESI†). The moment tensor potentials (MTPs) belong to the machine learning potentials and have been integrated into the Machine Learning Interatomic Potentials (MLIPs) package.[58,59] In this study, the MTPs were employed to obtain third-order IFCs. The *ab initio* molecular dynamics (AIMD) simulations were performed using a 3 × 3 × 3 supercell at temperatures of 50, 300, 500, 700, and 900 K,[60] each for 1 ps with a time step of 1 fs. The training set was derived from the complete simulation trajectories, with one configuration sampled every two time steps, which was then used to train the MTP models through passive training. The AIMD trajectories at multiple temperatures (50, 300, 500, 700 and 900 K) were originally generated to evaluate the thermal stability of the RbCaX (X = As, Sb) compounds, and were subsequently reused to train the MTP model, thereby avoiding additional DFT calculations. Anharmonic third-order IFCs were obtained with the same superlattice by considering the tenth nearest-neighbor atoms using the thirdorder_vasp.py code. In fact, the MTPs-based method for evaluating IFCs not only meets the accuracy of standard DFT calculations but also reduces expensive computational resources, as demonstrated in previous work.[58] To ensure convergence of phonon dispersion and lattice thermal conductivity, interactions up to the tenth nearest neighbor were included. The lattice thermal conductivity was computed by employing the complete iterative solutions of the Boltzmann transport equation, which encompass three-phonon scattering phenomena, as implemented in the ShengBTE code.[61,62] The convergence of scalebroad parameters, the Q-point mesh density, and the consideration of interactions up to the nearest neighbor are verified, as demonstrated in Fig. S12–S14 (ESI†).

3 Results and discussion

3.1 Equilibrium geometry and stability

The ternary RbCaAs and RbCaSb compounds fall within the I–II–V type semiconductor family and are structurally analogous to Cu_2Sb (PbClF)/KMnAs.[63,64] Both compounds crystallize in the centrosymmetric tetragonal symmetry space group $P4/nmm$ (No. 129) and possess similar atomic coordinates. They consist of four X atoms (X = As or Sb) positioned at the vertices of a tetrahedron centered around a Ca atom. These tetrahedral units are edge-sharing, forming a layered structure that extends in a specific direction, with the layers interconnected by Rb atoms, as illustrated in Fig. 1(a). In the out-of-plane direction, the RbCaX (X = As, Sb) compounds consist of alternating $[Ca_2X_2]^{2-}$ and $[Rb]^{2+}$, resulting in weak van der Waals (vdW) interactions between adjacent layers. The hierarchical bonded sublattice structure in RbCaX (X = As, Sb) compounds makes them inherently suited for low thermal conductivity. Table 1 presents the unit cell lattice parameters optimized using the PBE and PBESol methods with D3 dispersion correction. The calculated lattice parameters for RbCaAs and RbCaSb align well with experimental measurements,[41] where the PBE+D3 method shows a better match. Rb^{1+} and As^{3-} (Sb^{3-}) ions are coordinated in a square pyramidal with every Rb–As (Sb) bond length equal to ∼3.956 (∼4.078) Å, with the longer Rb–Sb bond lengths originating from the larger ionic radius of Sb atom. Additionally, despite shorter Ca–As bonds compared to Ca–Sb bonds, the vdW distances between $[Rb_2]^{2+}$ and $[Ca_2As_2]^{2-}$/$[Ca_2Sb_2]^{2-}$ layers in RbCaAs (∼1.538) is larger than RbCaSb (∼1.482 Å), suggest stronger interlayer interactions than classical van der Waals laminates.[65–67]

The different bond types in RbCaX (X = As, Sb) enhance the tunability of their chemical bonding. Fig. 1(b) shows the two-dimensional electron localization function (ELF) of these two materials on the (0 0 1) and (1 0 0) planes at 0 Å from the origin. According to the color scale in the figure from 0 (fully delocalized electrons) to 1 (fully localized electrons), the low electron localization around Ca atoms, compared to the stronger localization around Rb and As (Sb), indicates that Ca–As (Sb) bonding in the material has low electron sharing and is

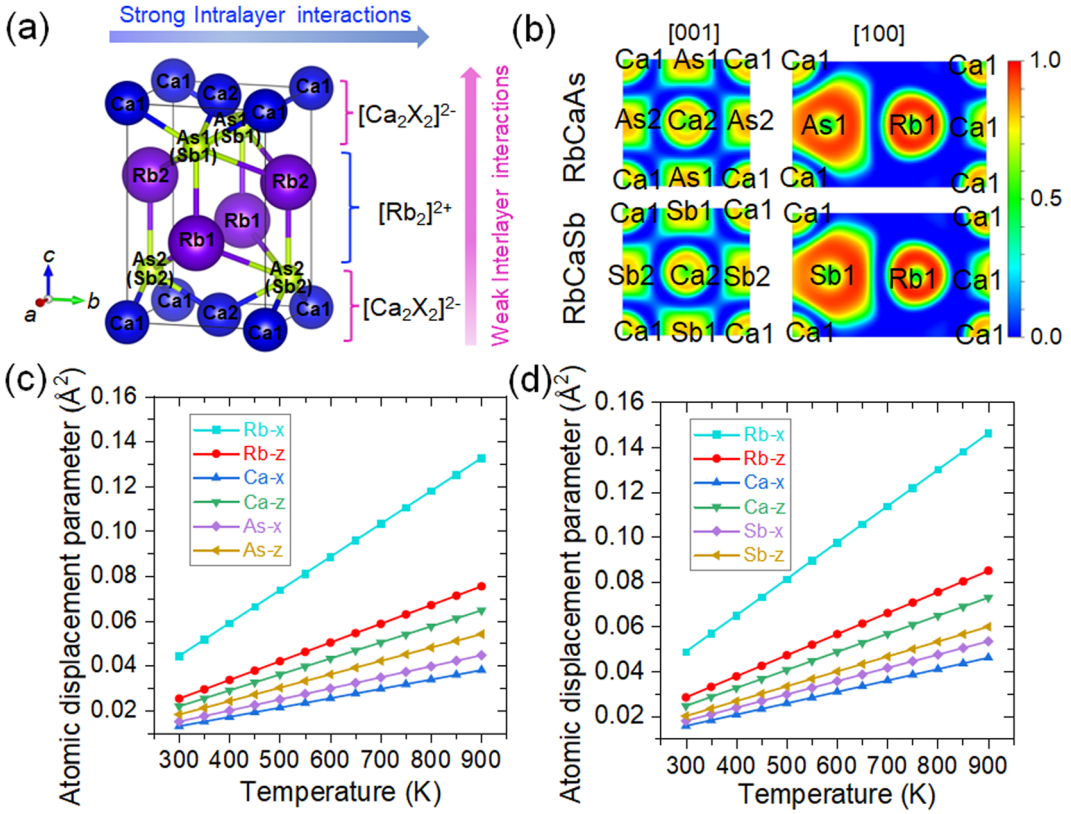

Fig. 1 (a) The crystal structures of layered RbCaX (X = As, Sb). (b) The electronic localization function (ELF) on the (001) and (100) planes for the RbCaAs and RbCaSb. The blue and red (ELF = 0.0 and 1.0) colours denote no electron localization and full electron localization, respectively. The atomic displacement parameter as a function of temperature for the (c) RbCaAs and (d) RbCaSb.

Table 1 The calculated crystal structure parameters of RbCaAs and RbCaSb, with % differences from the experimental data in parentheses. d_{layer} refers to the interlayer spacing

Functional	Compound	a/b (Å)	c (Å)	Ca–As/Sb (Å)	Rb–As/Sb (Å)	d_{layer} (Å)
PBE+D3	RbCaAs	5.154 (0.23%)	7.897 (−0.44%)	2.959 (−0.17%)	**3.956**	**1.538**
	RbCaSb	5.373 (0.19%)	8.503 (0.40%)	3.162 (0.13%)	**4.078**	**1.482**
PBEsol+D3	RbCaAs	5.093 (−0.95%)	7.737 (−2.46%)	2.923 (−1.38%)	3.897	1.490
	RbCaSb	5.300 (−1.17%)	8.355 (−1.35%)	3.122 (−1.14%)	4.012	1.432

dominated by ionic interactions. Conversely, Rb–As (Sb) bonding exhibits weak bonding characteristics due to the high localization of electrons around atoms. The bonding heterogeneity, characterized by weak interlayer vdW interactions and strong intralayer ionic bonding, reduces lattice rigidity and induces rattling-like behavior of Rb atoms. This limits phonon transport along the out-of-plane direction, resulting in lower thermal conductivity and significant anharmonicity. Further, Fig. 1(c) and (d) show that the Rb atoms exhibit the largest atomic displacement, promoting its intrinsic rattling-like behavior in RbCaX (X = As, Sb) compounds. Additionally, to further analyze the differences between intralayer and interlayer interactions, the charge density difference and Bader charge analyses were employed as complementary tools. These methods reveal the characteristics of various interactions in the material from the perspective of electronic structure, as illustrated in Fig. S1 and Table S1 (ESI†).

Using the PBE functional and python-ternary module, the convex hull energy diagrams of RbCaX (X = As, Sb) against other possible secondary phases in the Materials Project database were plotted, as shown in Fig. S2 (ESI†). The RbCaX (X = As, Sb) compounds are situated on the convex hull region, corresponding to the lowest dissociation energies (E_d) regions,[68] confirming their chemical stability in the *P*4/*nmm* space group relative to other secondary phases.

To gain deeper insights into the stability and mechanical behavior of RbCaX (X = As, Sb) compounds, the elastic properties were evaluated using the stress–strain method.[69] Given that the structures belong to the tetragonal crystal system, six independent elastic constants C_{ij} (C_{11}, C_{12}, C_{13}, C_{33}, C_{44}, and

C_{66}) have been determined according to Hook's law,[70] which is listed in Table S2 (ESI†). The RbCaX (X = As, Sb) compounds satisfy the mechanical stability criteria, *i.e.*, $C_{11} > 0$, $C_{33} > 0$, $C_{44} > 0$, $C_6 > 0$, $(C_{11} - C_{12}) > 0$, $(C_{11} + C_{33} - 2C_{13}) > 0$, $[2(C_{11} + C_{12}) + C_{33} + 4C_{13}] > 0$. Furthermore, considering that the C_{11} values (~44.56 and ~34.87 GPa) of RbCaX (X = As, Sb) are larger than C_{12} values (~5.14 and ~4.15 GPa), the shear constants were subsequently derived using the following formula:

$$C' = \frac{C_{11} - C_{12}}{2}, \quad (3)$$

as a result, the shear constants of RbCaAs and RbCaSb were found to be ~19.71 and ~15.36 GPa, which are much lower than some classical thermoelectric materials.[71,72] Generally, lowering the shear constant helps to reduce the phonon thermal conductivity, which is also confirmed later in the subsequent thermal transport calculations. From the calculated elastic constants, the bulk modulus, shear modulus and Young's modulus are derived by the Voigt–Reuss–Hill approach.[73–75] As portrayed in Table S2 (ESI†), the bulk modulus of RbCaX (X = As, Sb) is significantly higher than the shear modulus, leading to a relatively large Poisson's ratio (0.3). Such positive Poisson's ratio (0.3–0.5) suggests that when tensile stress is applied in one direction, the material contracts in the perpendicular directions. Coupled with the ELF analysis shown in Fig. 1(b), these findings confirm that both compounds exhibit typical ionic bonding characteristics. The B_H/G_H (toughness index) values for RbCaX (X = As, Sb) are ~2.16 and ~2.11, respectively, indicating ductility according to Pugh's scale.[76]

AIMD calculations were conducted to verify the thermal stability of RbCaX (X = As, Sb). Snapshots from AIMD simulation at 300, 500, 700, and 900 K over 5 ps trajectories (with a time step of 1 fs) using a 3 × 3 × 3 supercell are presented in Fig. S3 (ESI†). After reaching equilibrium using canonical ensemble (NVT), the total energy variation with simulation time indicates that the supercells are essentially free of major deformation during the AIMD simulations, and the slight energy fluctuations further demonstrate their high thermal stability. Therefore, 900 K is selected as a representative temperature for exploring the phonon, electron transport and thermoelectric performance.

3.2 Anisotropic thermoelectric figure of merit

Combining the electrical and thermal transport properties, the theoretical *ZT*s for RbCaX (X = As, Sb) under n-type regions were evaluated at different temperatures and carrier concentrations, the results reveal that the two compounds exhibit significant anisotropy thermoelectric performance, as shown in Fig. 2. At 900 K, the optimal *ZT* of n-type RbCaSb are ~1.71 (in the in-plane direction) and ~3.19 (in the cross-plane direction), respectively, which are significantly higher than ~0.54 and

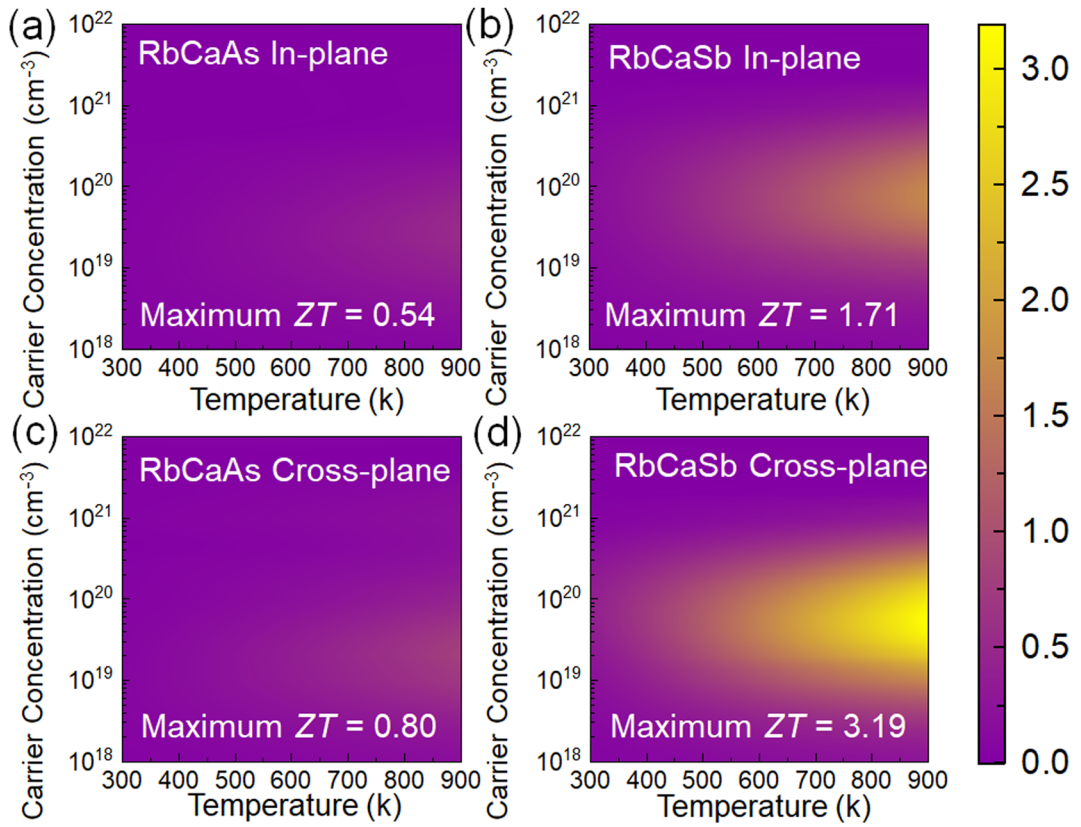

Fig. 2 Predicted thermoelectric figure of merit *ZT* of n-type (a), (c) RbCaAs and (b), (d) RbCaSb against temperature and carrier concentration along the in-plane and cross-plane directions. The lightest colors indicate the optimal *ZT*.

~0.80 of n-type RbCaAs, and also outperform the performance of typical layered TEs, such as p-type SnSe (ZT ~2.6, 923 K)[11] and BiCuOSe (predicted ZT ~0.75, 900 K).[77] To further explore the source of the superior thermoelectric performance of n-type RbCaSb over that of n-type RbCaAs, the electrical and thermal transport parameters of the two compounds are systematically analyzed in the following.

3.3 Electronic and transport properties

To comprehend the electrical transport properties of RbCaX (X = As, Sb), the electronic band structures and density of states (DOS) were calculated using the HSE06+D3 method depicted in Fig. 3(a) and (b). The Fermi energy level of RbCaX (X = As, Sb) was set to be 0 eV to separate the valence band maximum (VBM) from the conduction band minimum (CBM). Specifically, RbCaAs and RbCaSb exhibit indirect band gap of ~2.01 eV and ~2.19 eV, respectively, with both the CBMs located at the Γ point and predominantly contributed by the As/Sb-p orbitals, whereas the VBMs are situated along the M–Γ and A–Z directions, dominated by the hybridization of As/Sb-d and Ca-d orbitals. These bandgaps are wider than those of BiSb (~1.67 eV)[78] and SnSe (~1.28 eV)[79] and are therefore more resistant to the bipolar conduction effect[80] that typically occurs at high temperatures and degrades TE performance. Additionally, the extended Rb–As/Sb interatomic distance weakens out-of-plane interactions, leading to suppressed band dispersion along the Γ–Z direction near the Fermi level. Conversely, strong in-plane bonding interactions enhance band dispersion along the Γ–X and Γ–M directions. The combination of flat and dispersive energy bands within the electronic band structure of layered RbCaAs and RbCaSb compounds are highly advantageous for achieving a large Seebeck coefficient and high electron mobility. The VBMs of two materials are found to be flat in reciprocal space (*i.e.*, short-range interactions in real space), leading to large peaks in the partial density of states (PDOS), which suggests a high Seebeck coefficient for p-type doping. In contrast, the CBMs are dispersive, implying a lighter effective mass and higher velocity of the electron population, thus indicating high electrical conductivity for n-type doping. The As/Sb atoms mainly contribute to the PDOS peaks, as these two atoms are important players involved in the bonding (see Fig. 1(b)).

Due to the moderate electronic band gap, pristine RbCaX (X = As, Sb) exhibit relatively low thermal electron and hole populations at ambient temperature compared to narrow band-gap semiconductors. Nonetheless, high carrier concentrations (~10^{21} cm^{-3}) are achievable in such materials through doping (*e.g.*, Cl or Na doped $PbSnS_2$),[81] a focus of active semiconductor research. Inspired by the small effective mass of electrons, electron transport simulations were performed in this study under n-type regions with the carrier concentration range of 10^{18}–10^{21} cm^{-3} and temperatures between 300–900 K. According to convergence tests, the electronic transport calculations of n-type RbCaX (X = As, Sb) converge with an interpolation factor of 50 using a 12 × 12 × 8 k-mesh (see Fig. S4–S7, ESI†).

Based on DFT calculations of electron (see Fig. 3), phonon, and electron–phonon coupling properties (see Fig. 4, for a detailed analysis of the phonon spectrum was presented later in the section on calculations of thermal transport properties), the carrier mobility was determined using the Boltzmann transport equation employed in the AMSET package. The variation of carrier scattering rates of n-type RbCaAs and n-type RbCaSb at specific carrier concentrations (n_e = 2 × 10^{19} and 5 × 10^{19} cm^{-3}) and temperature (900 K) was studied (corresponding to the optimal ZT), and the results are displayed in Fig. 5.

In Fig. 5(a) and (d), the average scattering rates of n-type RbCaAs and n-type RbCaSb are demonstrated as a function of temperature for fixed carrier concentrations of n_e = 2 × 10^{19} cm^{-3} and 5 × 10^{19} cm^{-3}, respectively. For both compounds, the POP (carrier scattering by dipoles induced by optical phonon vibrations) scattering gradually dominates with increasing temperature. In contrast, IMP (caused by charged lattice defects) scattering remains relatively constant within this temperature range. As the temperature rises, the total scattering rate increases due to the enhancement of POP and ADP scatterings. It is noteworthy that the total scattering rate of n-type RbCaSb is significantly lower than that of n-type RbCaAs, mainly due to its larger high-frequency dielectric constant (see Table S2, ESI†), which is conducive to achieving higher

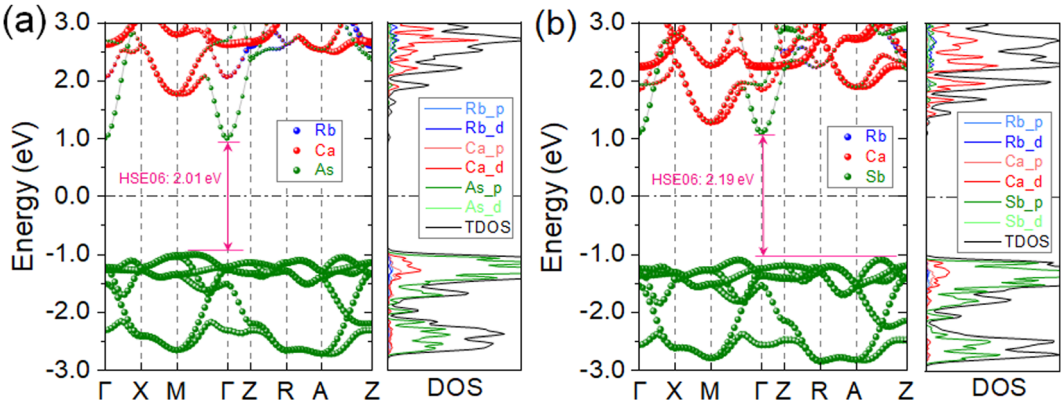

Fig. 3 Calculated the electronic band structures and density of states (DOS) for the (a) RbCaAs and (b) RbCaSb.

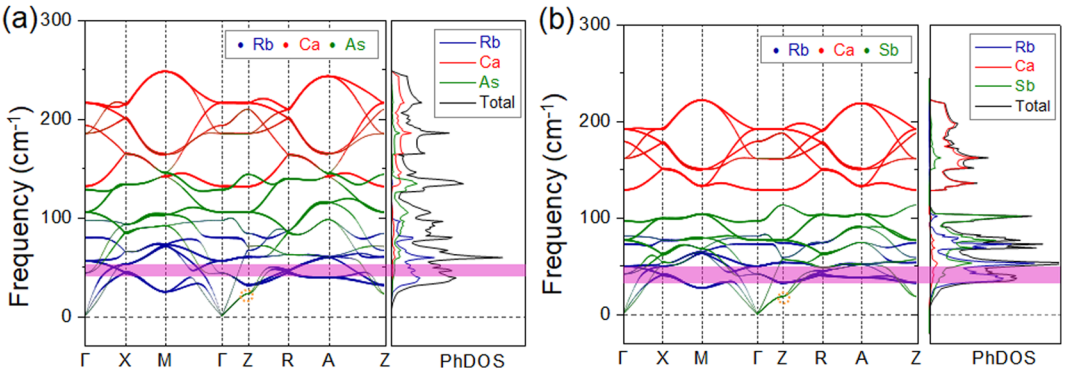

Fig. 4 Phonon dispersion together with corresponding phonon density of states (PhDOS) curves of (a) RbCaAs and (b) RbCaSb. The blue, red, and green lines represent the contributions of Rb, Ca, and X (X = As, Sb) atoms, respectively. The yellow dashed circle marks the phonon softening at the *Z* point.

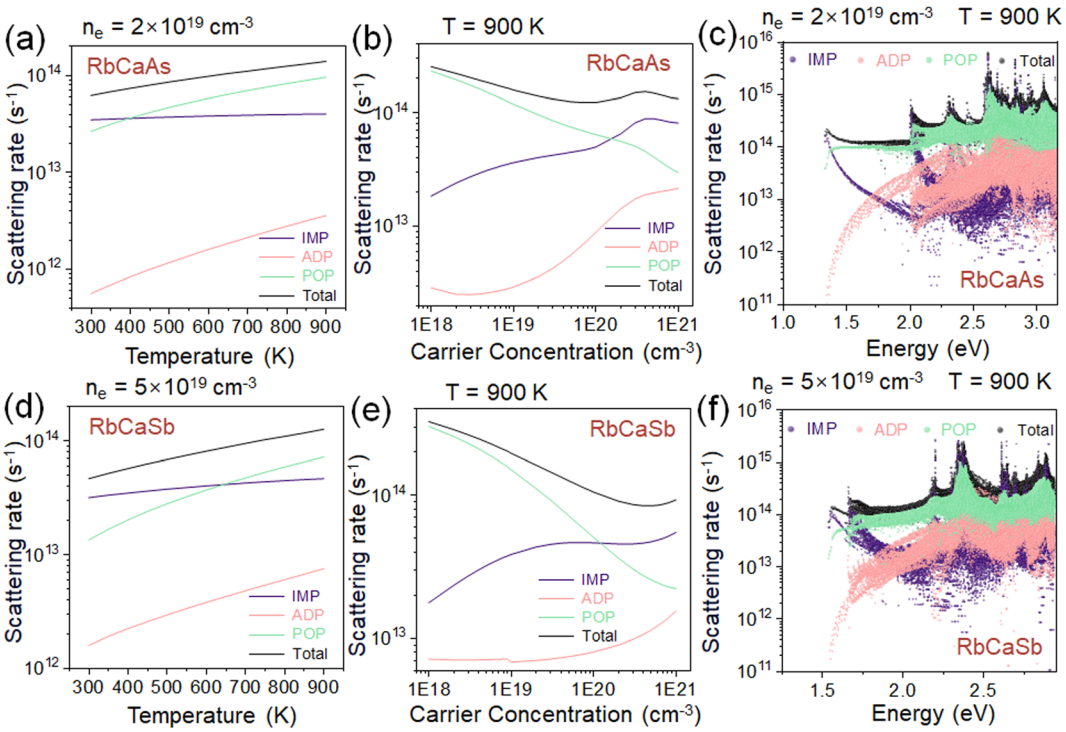

Fig. 5 Average scattering rates for n-type RbCaAs and RbCaSb, where carrier concentration/temperature are fixed to the values that give the maximum predicted *ZT*, (a), (c) shown as a function of temperature for a fixed n_e = 2 × 10^{19} cm^{-3} and 5 × 10^{19} cm^{-3} and (b), (d) as a function of charge carrier concentration for a fixed *T* = 900 K. The n_e denotes the carrier concentration of n-type regions.

conductivity. On the other hand, Fig. 5(b) and (e) demonstrate the trend of the average scattering rate with carrier concentration at a fixed temperature of *T* = 900 K. At low carrier concentrations, POP scattering dominates the scattering rates of n-type RbCaAs and n-type RbCaSb. As the carrier concentration increases, IMP scattering gradually becomes dominant because these defects are both scattering centers and sources of free carriers. IMP scattering enhances with increasing doping concentration and eventually stabilizes, and its behavior is essentially temperature-independent. While ADP scattering contributes the least to the total scattering rate, in contrast, the contribution of ADP scattering is slightly higher for n-type RbCSb than for n-type RbCaAs, which can be explained by the higher deformation potentials (∼0.43 eV in the *xy*-plane and ∼1.09 eV along the *z*-direction for n-type RbCaSb, compared to ∼0.42 eV and ∼0.76 eV for n-type RbCaAs). ADP scattering arises from lattice vibrations induced by electron-acoustic phonon interactions, leading to localized strain that disturbs the energy bands and scatters carriers. The scattering rate can also be described as a function of energy. Fig. 5(c) and (f) show the normalized scattering rate as a function of energy at the temperature (*T* = 900 K) and carrier concentration

($n_e = 2 \times 10^{19}/5 \times 10^{19}$ cm^{-3}) corresponding to the optimal *ZT*, respectively. At the edge of the conduction band, IMP scattering reaches higher scattering rates in both compounds, significantly exceeding ADP scattering. In the higher energy range, POP scattering dominates, exhibiting significantly higher scattering rates than other scattering mechanisms in the ~1.5 eV to ~3.0 eV. The total scattering rate of n-type RbCaAs is slightly higher than that of n-type RbCaSb over the whole energy range, which is one of the reasons for the higher electrical conductivity of n-type RbCaSb. Additionally, the dominant scattering mechanism varies between POP, IMP, and ADP scattering, as affected by doping concentration and temperature. Overall, under the temperature and carrier concentration regions corresponding to the optimal *ZT*, IMP and POP scattering are the main mechanisms for n-type RbCaAs and n-type RbCaSb.

To further investigate the difference in electron transport parameters between RbCaAs and RbCaSb, the temperature dependence of the electron thermal conductivity (K_e), electrical conductivity (σ), Seebeck coefficient (S), and power factor ($S^2\sigma$) at carrier concentrations of 1×10^{18}, 1×10^{19}, 1×10^{20}, and 1×10^{21} cm^{-3} were calculated under the n-type regions, as illustrated in Fig. 6. Among the four electronic transport properties, RbCaX (X = As, Sb) compounds exhibit lower electronic thermal conductivity at the optimal *ZT* in the n-type region due to their layered structure. Consistent with the Wiedemann–Franz law ($K_e = L\sigma T$, where L and T represent the Lorentz number and temperature, respectively), the trend in σ closely mirrors that of K_e. Meanwhile, the electrical conductivity decreases with increasing temperature of n-type RbCaX (X = As, Sb). However, this decline becomes more moderate at high carrier concentrations, as the dominant contribution of temperature-independent IMP scattering, outweighs the effect of ADP scattering in the total scattering rate.

The Seebeck coefficient (S) quantifies the voltage generated over a temperature gradient, with its sign determined by the dominant carrier type: positive for holes and negative for electrons. The magnitude of S depends on the energy distribution of carriers and the chemical potential. Typically, the trend of S with temperature can be described by the degenerate Fermi gas model:[82]

$$S = \frac{8\pi^2 k_B^2}{3eh^2} m^*_{DOS} T \left(\frac{\pi}{3n}\right)^{2/3}, \quad (4)$$

where k_B is the Boltzmann constant, e represents the elementary charge, h denotes Planck's constant, n is the carrier concentration, and m^*_{DOS} represents the DOS effective mass. The S typically exhibits a temperature and carrier concentration dependence opposite to the σ, decreasing with increasing carrier concentration and rising with temperature. This behavior arises from carrier diffusion and the resulting voltage difference across temperature gradients. Under n-type regions, RbCaSb consistently outperforms RbCaAs in S, displaying a marked contrast to their electrical conductivity trends. Remarkably, n-type RbCaSb sustains a high S (~200 μV K^{-1}) even at elevated carrier concentration ($n = 1 \times 10^{19}$ cm^{-3}) and room temperature (300 K). This suggests that n-type RbCaSb has greater potential as an efficient thermoelectric material, as $S \geq 200$ μV K^{-1} is regarded as a key criterion for thermoelectric candidates.[83]

The power factor ($PF = S^2\sigma$) is a critical parameter for assessing thermoelectric performance ($ZT \propto PF$). Since the intrinsic trade-off between the Seebeck coefficient (S) and

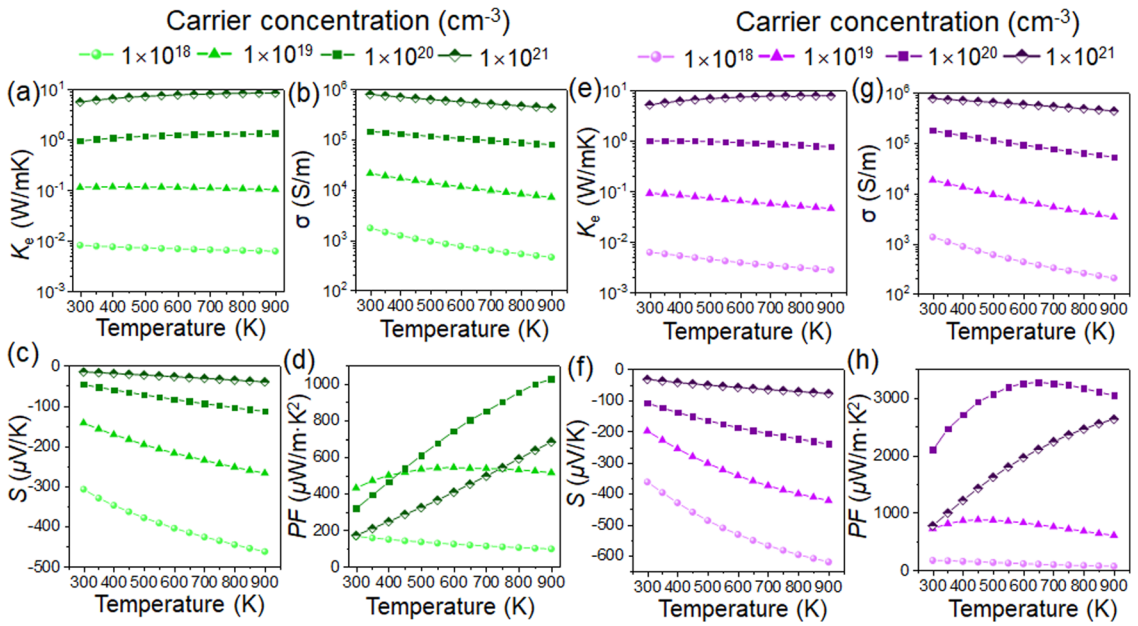

Fig. 6 Calculated electronic transport properties as a function of temperature for n-type (a)–(d) RbCaAs and (e)–(h) RbCaSb at four different carrier concentrations. Here, K_e represents electronic contribution to the thermal conductivity, while K_l denotes the phononic contribution. σ stands for the electrical conductivity, S is the Seebeck coefficient, and PF represents the power factor ($S^2\sigma$).

Table 2 Predicted optimal *ZT* in n-type RbCaX (X = As, Sb) along the in-plane and cross-plane directions together with corresponding charge carrier concentration (*n*), temperature (*T*, K), Seebeck coefficient (*S*, μV K^{-1}), electrical conductivity (*σ*, S m^{-1}), electronic thermal conductivity (K_e, W m^{-1} K^{-1}) and power factor (*PF*, μW m^{-1} K^{-2})

System	Type	Direction	*ZT*	*n* (cm^{-3})	*T* (K)	*S* (μV K^{-1})	*σ* (S m^{-1})	K_e (W m^{-1} K^{-1})	*PF* (μW m^{-1} K^{-2})
RbCaAs	n-Type	*xy*	0.54	3×10^{19}	900	−184.56	27 876.11	0.49	949.50
	n-Type	*z*	0.80	2×10^{19}	900	−211.73	12 364.05	0.23	554.3
RbCaSb	n-Type	*xy*	**1.71**	8×10^{19}	900	−247.91	**39 081.67**	0.62	**2401.99**
	n-Type	*z*	**3.19**	5×10^{19}	900	−306.51	**26 651.24**	0.39	**2503.81**

electrical conductivity (*σ*) as a function of carrier concentration, the calculation of *PF* aims to achieve an optimal balance between these two quantities. The *PF* of n-type RbCaAs reaches ∼1.03 mW m^{-1} K^{-2}, while n-type RbCaSb exhibits a higher *PF* of ∼3.28 mW m^{-1} K^{-2}. The electronic transport properties for both in-plane and cross-plane directions are detailed in Fig. S8 and S9 (ESI†). Notably, the anisotropy of *PF*s between these two directions is more pronounced in both compounds (especially n-type RbCaAs) compared to *σ*, K_e, and *S*. Table 2 further reveals that the in-plane and cross-plane *PF*s for n-type RbCaSb are both ∼2.5 mW m^{-1} K^{-2}, substantially exceeding the n-type RbCaAs (∼0.95 and ∼0.55 mW m^{-1} K^{-2}, respectively) at the optimal *ZT*. These elevated *PF*s of n-type RbCaSb are primarily attributed to its enhanced *S* and *σ*.

3.4 Thermal transport properties

The following part focuses on exploring the differences in the thermal transport parameters between the RbCaAs and RbCaSb. Prior to calculating phonon thermal transport properties, the lattice conductivity at room temperature was verified to converge with the scalebroad factor, the Q-point grid density, and the number of nearest-neighbour atoms. A scalebroad factor of 1.0, a 20 × 20 × 20 Q-point grid, and inclusion up to the 10th nearest-neighbor atoms were ultimately selected, as shown in Fig. S12–S14 (ESI†). The lattice thermal conductivity (K_l) of two compounds, as illustrated in Fig. 7(a), decreases with increasing temperature due to enhanced phonon–phonon scattering at higher temperatures. Owing to strong intralayer bonding and weak interlayer bonding, RbCaAs and RbCaSb

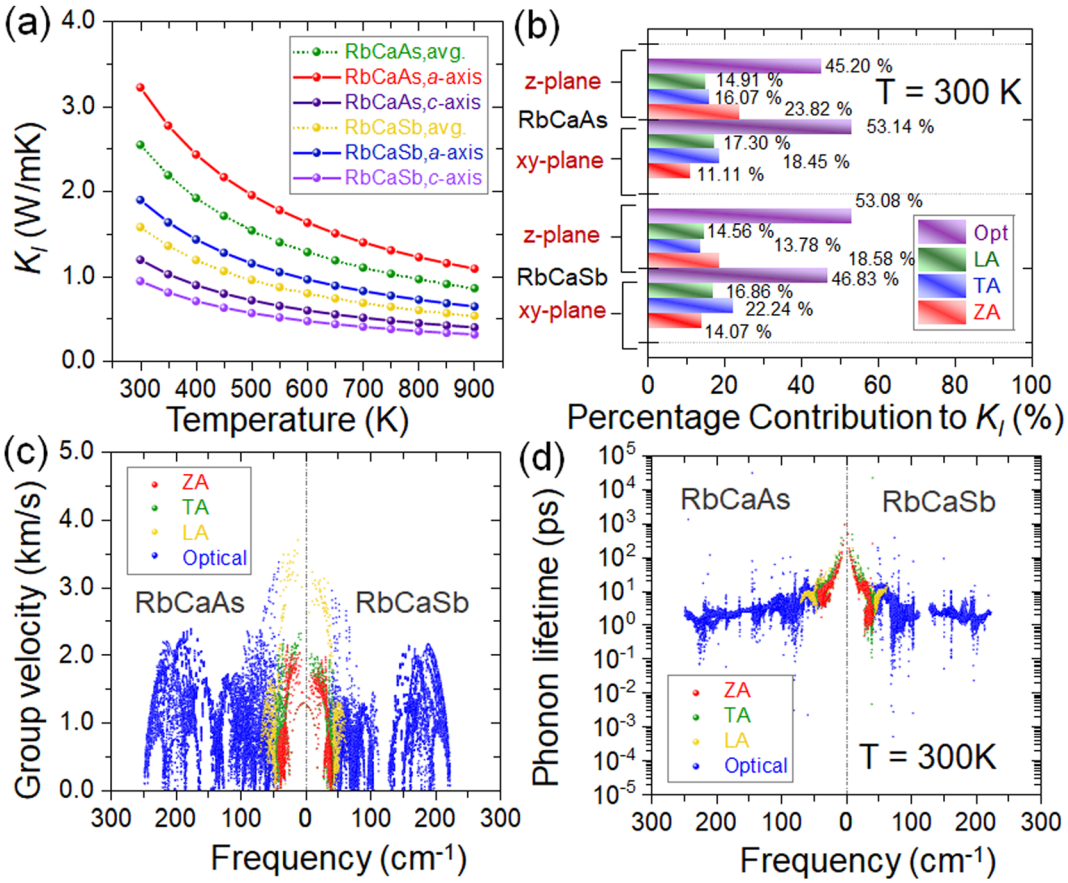

Fig. 7 (a) Calculated lattice thermal conductivity (K_l) as a function of temperature. (b) Percentage contribution of phonon modes to total lattice conductivity for RbCaX (X = As, Sb) at 300 K along both directions. (c) Calculated phonon group velocity and (d) phonon lifetime of RbCaAs and RbCaSb as a function of phonon frequency.

exhibit significant anisotropy in lattice thermal conductivities between the interlayer (*c*-axis) and intralayer (*a*/*b*-axis) directions, with $K_{l(x,y)}/K_{l(z)}$ ratios of ~2.70 and ~2.01, respectively. At 300 K and 900 K, the average lattice thermal conductivity of RbCaSb is ~1.6 W m^{-1} K^{-1} and ~0.5 W m^{-1} K^{-1}, comparable to other layered thermoelectric materials such as BiCuOSe (~1.0 W m^{-1} K^{-1} at 300 K),[77] but lower than that of RbCaAs (~2.5 W m^{-1} K^{-1} and ~0.9 W m^{-1} K^{-1}). The behavior can be rationalized by analyzing the phonon dispersion in Fig. 4. Given their structural and compositional similarities, both compounds exhibit comparable phonon dispersions, featuring relatively flat bands that suggest low phonon group velocities and lattice thermal conductivities. Notably, the ZA and TA modes of the RbCaX (X = As, Sb) compounds exhibit pronounced softening at the Z point, reducing the phonon group velocity along the out-of-plane (Γ–Z) direction. This effect arises from weak interlayer van der Waals interactions. Due to its weak bonding with the crystal lattice, the Rb atom in RbCaAs and RbCaSb manifests distinct localized phonon modes in the low-frequency ranges (~38.89 to ~52.10 and ~33.07 to ~49.24 cm^{-1}, see the magenta area in Fig. 4), indicative of rattling-like behavior. These localized modes enhance phonon scattering, restrict free phonon propagation, and shorten the effective mean free path, thereby reducing lattice thermal conductivity. The highest acoustic mode frequencies of RbCaAs and RbCaSb are ~71 cm^{-1} and ~63 cm^{-1}, respectively, comparable to state-of-the-art thermoelectric material SnSe,[84] reflecting mode softening phenomena. This feature facilitates strong coupling between the acoustic and low-frequency optical modes, enhancing the phonon scattering effect. It is noteworthy that the heavy Rb and X (As/Sb) atoms jointly contribute to the acoustic and low-frequency optical modes (< 150 cm^{-1}), while the lighter Ca atoms dominate the high-frequency optical modes. Since Sb (121.7 amu) is heavier than As (74.9 amu), RbCaSb exhibits a greater phonon density of states in the low-frequency acoustic range (0 to ~63 cm^{-1}) compared to RbCaAs, which enhances phonon scattering and consequently reduces lattice thermal conductivity (the average lattice thermal conductivity of RbCaAs at 300 K is ~1.5 times higher than RbCaSb). Additionally, the absence of imaginary frequencies in the harmonic phonon calculations confirms the dynamic stability of both compounds.

To further reveal the potential mechanisms of the low K_l in RbCaAs and RbCaSb, the contributions of different phonon branches to K_l along the interlayer and intralayer directions at 300 K are presented in Fig. 7(b). In the interlayer direction of RbCaAs and the intralayer direction of RbCaSb, the acoustic phonon contribution exceeds approximately 50%. In contrast, in the intralayer direction of RbCaAs and RbCaSb, the contribution from optical phonons (Opt) is slightly larger. Overall, the coupling between acoustic and optical modes results in a relatively low lattice thermal conductivity of the two compounds.

This behavior is intrinsically related to the interatomic force constants (IFCs), which play a key role in determining the K_l. This study investigates the impact of second- and third-order IFCs on lattice thermal conductivity, with the second-order IFCs obtained *via* the finite difference method and the third-order IFCs derived from first-principles calculations combined with machine learning. Based on the IFCs, the lattice thermal conductivity is determined by summing the contributions from each phonon mode, using the following formula:

$$K_l = \frac{1}{NV}\Sigma_\lambda C_\lambda v_\lambda \otimes v_\lambda \tau_\lambda \quad (5)$$

where N refers to the number of wavevectors (equivalent to the number of unit cells), and V is the unit cell volume. The modal heat capacity, group velocity, and phonon lifetime are denoted by C_λ, v_λ, and τ_λ, respectively. To further investigate the thermal transport mechanism, variations in phonon group velocity and phonon lifetime with respect to frequency are examined within the single-mode relaxation time approximation (RTA). The phonon group velocity can be obtained by using the phonon spectrum,

$$v_i = \frac{\partial \omega_i}{\partial q} \quad (6)$$

where ω_i and q denote the phonon frequency of the i-th vibrational mode and the associated wave vector, respectively. As shown in Fig. 7(c), most phonon group velocities in RbCaAs and RbCaSb range from 0 to ~4 km s^{-1}. Higher group velocities are observed in the frequency range of ~4 to ~75 cm^{-1} in RbCaSb (with a maximum of about ~3.23 km s^{-1}), whereas in RbCaAs the range is broader spanning ~4 to ~100 cm^{-1} (with a maximum of about ~3.70 km s^{-1}). The proportion of phonon modes with high group velocities is lower in RbCaSb than in RbCaAs, which may be attributed to the localization of phonon modes induced by Sb. On the other hand, the phonon lifetime is jointly determined by several scattering mechanisms according to Mathieson's rule:[85]

$$\frac{1}{\tau_\lambda} = \frac{1}{\tau_\lambda^{anh}} + \frac{1}{\tau_\lambda^{iso}} + \frac{1}{\tau_\lambda^{B}} \quad (7)$$

where τ_λ denotes the phonon lifetime, whose inverse is the scattering rate, which comprises the contributions from intrinsic anharmonic phonon–phonon scattering rate ($1/\tau_\lambda^{anh}$), isotopic phonon scattering rate ($1/\tau_\lambda^{iso}$), and phonon-boundary scattering rate ($1/\tau_\lambda^{B}$). As illustrated in Fig. 7(d) and Fig. S15(a) (ESI†), the phonon lifetimes of RbCaAs and RbCaSb are predominantly distributed in the range of 10^{-1} to 10^{2} ps (at 300 K) and 10^{-1} to 10^{1} ps (at 900 K). Longer phonon lifetimes occur in the low-frequency range (~4 to ~71 cm^{-1} for RbCaAs and ~4 to ~63 cm^{-1} for RbCaSb). At 300 K, the mid-frequency phonon modes (~4 to ~71 cm^{-1} for RbCaAs and ~4 to ~63 cm^{-1} for RbCaSb) and the high-frequency Ca-based phonon modes (~130 to ~249 for RbCaAs and ~115 to ~223 cm^{-1} for RbCaSb) typically have lifetimes below 10 ps. At 900 K, these phonon lifetimes further decrease, with 68% and 78% in the mid- and high-frequency ranges (~71 to ~249 cm^{-1} for RbCaAs and ~63 to ~223 cm^{-1} for RbCaSb) having lifetimes below 1 ps, reflecting strong phonon–phonon scattering and high anharmonicity, resulting in a lower K_l.

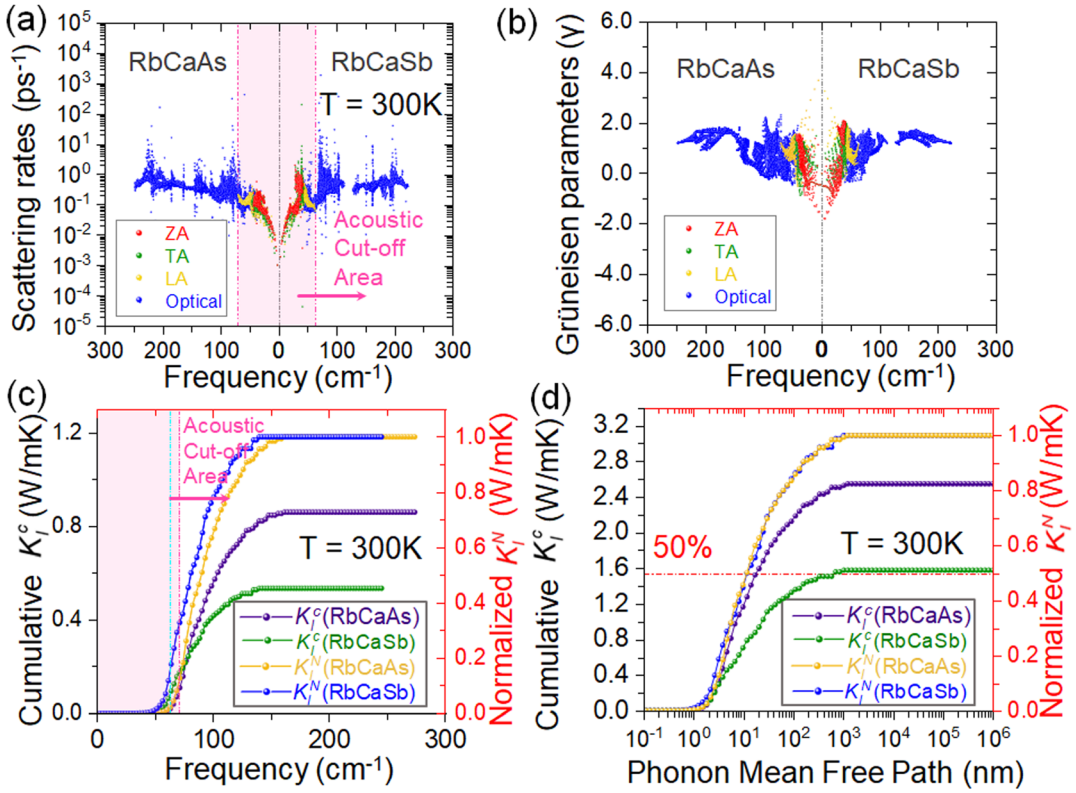

Fig. 8 (a) Calculated three-phonon scattering rates and (b) Grüneisen parameter (γ) as a function of phonon frequency for RbCaAs and RbCaSb. (c) Cumulative and normalized lattice thermal conductivity (K_l^C and K_l^N) as a function of phonon frequency at 300 K for RbCaX (X = As, Sb). The pink area represents the acoustic cut-off area. (d) Cumulative and normalized lattice thermal conductivity (K_l^C and K_l^N) as a function of phonon mean free path at 300 K for RbCaX (X = As, Sb). The red dashed line shows the thermal conductivity suppression to 50%.

Based on the phonon lifetime, the phonon scattering rate spectrum at 300 K was calculated (see Fig. 8(a)). The pink-shaded regions indicate the phonon cutoff frequency range (~4 to ~71 cm^{-1} for RbCaAs and ~4 to ~63 cm^{-1} for RbCaSb), *i.e.*, the low-frequency region. It is dominated by the ZA (zeroth acoustic), TA (transverse acoustic), and LA (longitudinal acoustic) acoustic phonon modes, which exhibit low scattering rates. In contrast, high-frequency optical modes (blue-shaded area) have higher scattering. Moreover, stronger optical and acoustic phonon resonance effects increase the scattering rate in the low-frequency region and the scattering channel of the heat-carrying acoustic phonons, as confirmed by the fact that RbCaSb has a larger scattering rate and lower K_l than RbCaAs (see Fig. 8(a)). At 900 K, the frequency-dependent trend of the scattering rates remains similar to that of 300 K, but the peak scattering rate significantly increases (see Fig. S15(b), ESI†).

Furthermore, to further assess the bond anharmonicity of RbCaAs and RbCaSb, the mode Grüneisen parameter (γ) and average Grüneisen parameters are calculated using the following equation:[57]

$$\gamma_i = -\frac{V_0}{\omega_i}\frac{\partial \omega_i}{\partial V} \quad (8)$$

where ω_i is the phonon frequency of i-th mode in equilibrium volume (V_0), and γ_i characterizes the relationship between phonon frequency and crystal volume change. As displayed in Fig. 8(b), the phonon mode Grüneisen parameters of RbCaAs and RbCaSb are positive, with the highest γ values concentrated in the acoustic and low-frequency optical branches. This suggests that the strong acoustic-optical coupling enhances anharmonic scattering within a narrow frequency range (~4 to ~100 cm^{-1}). The average Grüneisen parameters, calculated at 300 K (900 K) obtained based on the method given in Shao *et al.*[86], are ~0.82 (~0.97) and ~1.04 (~1.15) for RbCaAs and RbCaSb, respectively, which are comparable to those of state-of-the-art TE materials such as PbTe (~1.49).[87] In summary, RbCaAs and RbCaSb exhibit comparable range of phonon group velocities, while the shorter phonon lifetime in RbCaSb with greater anharmonic scattering supports its lower K_l.

Fig. 8(c) demonstrates the cumulative lattice thermal conductivity (K_l^C) and normalized lattice thermal conductivity (K_l^N) as a function of phonon frequency at 300 K. At the acoustic cutoff frequency, the K_l^C values for RbCaAs and RbCaSb are ~0.01 W m^{-1} K^{-1} and ~0.02 W m^{-1} K^{-1}, respectively. Notably, the contribution of optical modes to K_l significantly exceeds that of acoustic modes, likely due to phonon scattering arising from the coupling between low-frequency optical and acoustic modes (see Fig. 8(a)). This characteristic persists at 900 K (see Fig. S15(c), ESI†). As the temperature increases to 900 K, the K_l^C at the acoustic cutoff frequency increases to ~0.11 W m^{-1} K^{-1} for RbCaAs and ~0.10 W m^{-1} K^{-1} for RbCaSb. To assess the

dimensional constraints on experimental crystals, the K_l^C and K_l^N as functions of the phonon mean free path (MFP) were calculated at 300 K, as shown in Fig. 8(d). The results indicate that the curves converge to 1.0 at long MFPs, demonstrating that the wavevector mesh is sufficiently fine for accurate results. At 300 K, phonons with MFPs ~11.78 nm contribute 50% of the total K_l for RbCaX (X = As, Sb). This suggests that crystals of similar size can effectively suppress phonons contributing 50% of K_l, as phonons with mean free paths exceeding this dimension exhibit ballistic transport and are limited by the size effect[88]. At 900 K, the MFPs corresponding to 50% of K_l^C reduce to ~3.85 nm, reflecting the enhanced phonon scattering at elevated temperatures. This trend is further confirmed by comparing the relationship between frequency and scattering rate at 300 K and 900 K (see Fig. 8(a) and Fig. S15(b), ESI†). These findings provide valuable guidance for experimental design, particularly in optimizing thermal conductivity by tailoring crystal dimensions.

4 Conclusions

In conclusion, the electronic structure, thermal transport, electrical transport and TE properties of RbCaX (X = As, Sb) are systematically investigated in combination with the semi-empirical Boltzmann transport equation and first-principles calculations, confirming their potential as n-type TE material in the medium- to high-temperature applications. At 900 K and a carrier concentration of $\sim 10^{19}$ cm^{-3}, the optimal anisotropy *ZT* values are ~0.54/~0.80 for RbCaAs and ~1.71/~3.19 for RbCaSb (in-plane/cross-plane), respectively. Based on the HSE06 hybrid functional, RbCaAs and RbCaSb are identified as wide bandgap indirect semiconductors with band gaps of ~2.01 and ~2.19 eV, respectively. Structural phase diagrams, elastic constants, AIMD simulations, and phonon dispersions verify their chemical, mechanical, thermal and dynamic stability.

The weak anisotropy of the electrical transport properties of the two compounds is mainly influenced by ADP, IMP and POP scattering mechanisms, which endow them with a high *PF*. Among them, n-type RbCaSb has a significantly better *PF* than n-type RbCaAs due to its higher Seebeck coefficient and conductivity at the temperature and carrier concentration corresponding to the optimal *ZT*. The high *ZT* can be attributed to the intrinsically low lattice thermal conductivity of the material. Both compounds exhibit intrinsically low average lattice thermal conductivity due to the rattling-like behavior induced by weak bonding of Rb–As/Sb, with RbCaSb (~1.90/0.94 W m^{-1} K^{-1} at 300 K along the *x*-/*y*-direction) lower than RbCaAs (~3.22/1.20 W m^{-1} K^{-1} at 300 K along the *x*-/*y*-direction), attributed to heavier Sb atoms enhancing anharmonic phonon–phonon scattering. Weak interlayer bonding enhances anharmonic scattering, significantly reduces the lattice thermal conductivity in the *z*-axis direction, and increases the anisotropy between in-plane and cross-plane. These findings demonstrate that RbCaX (X = As, Sb) are promising wide-bandgap thermoelectric materials. Compared with RbCaAs, which shows moderate thermoelectric performance, RbCaSb exhibits excellent thermoelectric performance at elevated temperatures, making it a strong candidate for waste heat recovery in lithium-ion battery thermal management systems.

Author contributions

Jingyi Zhang: writing – original draft, methodology, formal analysis, data curation, conceptualization. Junhao Peng: data curation, methodology, software. Runqing Zhang: data curation, formal analysis. Yanwei Liang: methodology, software. Zihan Xu: data curation. Renhai Wang: formal analysis. Fugen Wu: formal analysis, supervision. Da Wan: methodology, validation. Peifei Zhang: validation. Shulin Bai: methodology. Huafeng Dong: conceptualization, formal analysis, funding acquisition, methodology, supervision, writing – review & editing.

Conflicts of interest

There are no conflicts to declare.

Data availability

The data that support the findings of this study are available within this article.

Acknowledgements

This work was supported by the National Natural Science Foundation of China (grant no. 11604056). The authors thank the Center of Campus Network & Modern Educational Technology, Guangdong University of Technology, Guangdong, China, for providing computational resources and technical support for this work.

References

1 X. Zhang and L. D. Zhao, Thermoelectric materials: Energy conversion between heat and electricity, *J. Materiomics*, 2015, **1**, 92–105.
2 Y. Qin, B. Qin and D. Wang, *et al.*, Solid-state cooling: thermoelectrics, *Energy Environ. Sci.*, 2022, **15**, 4527–4541.
3 Z. Liu, W. Gao and F. Guo, *et al.*, Challenges for thermoelectric power generation: from a material perspective, *Mater. Lab.*, 2022, **1**, 220003.
4 Y. Qin, B. Qin and T. Hong, *et al.*, Grid-plainification enables medium-temperature PbSe thermoelectrics to cool better than Bi_2Te_3, *Science*, 2024, **383**, 1204–1209.
5 F. J. DiSalvo, Thermoelectric cooling and power generation, *Science*, 1999, **285**, 703–706.
6 L. M. Daniels, S. N. Savvin and M. J. Pitcher, *et al.*, Phonon-glass electron-crystal behaviour by A site disorder in n-type thermoelectric oxides, *Energy Environ. Sci.*, 2017, **10**, 1917–1922.

7 J. Qi, B. Dong and Z. Zhang, *et al.*, Dimer rattling mode induced low thermal conductivity in an excellent acoustic conductor, *Nat. Commun.*, 2020, **11**, 5197.
8 S. Bai, H. Shi and Y. Wen, *et al.*, Lattice vibrational hierarchy and Mean-Free-Path filtering in $Bi_6Cu_2Se_4O_6$ superlattice thermoelectrics, *Phys. Rev. X*, 2025, DOI: **10.1103/44gy-zmbf**.
9 Q. Jin, S. Jiang and Y. Zhao, *et al.*, Flexible layer-structured Bi_2Te_3 thermoelectric on a carbon nanotube scaffold, *Nat. Mater.*, 2018, **18**, 62–68.
10 X. Chen, H. Wu and J. Cui, *et al.*, Extraordinary thermoelectric performance in n-type manganese doped Mg_3Sb_2 Zintl: High band degeneracy, tuned carrier scattering mechanism and hierarchical microstructure, *Nano Energy*, 2018, **52**, 246–255.
11 L. D. Zhao, S. H. Lo and Y. Zhang, *et al.*, Ultralow thermal conductivity and high thermoelectric figure of merit in SnSe crystals, *Nature*, 2014, **508**, 373–377.
12 L. D. Zhao, D. Berardan and Y. L. Pei, *et al.*, $Bi_{1-x}Sr_xCuSeO$ oxyselenides as promising thermoelectric materials, *Appl. Phys. Lett.*, 2010, **97**, 092118.
13 S. Liu, S. Bai and Y. Wen, *et al.*, Quadruple-band synglisis enables high thermoelectric efficiency in earth-abundant tin sulfide crystals, *Science*, 2025, **387**, 202–208.
14 S. Bai, D. Liu and H. Shi, *et al.*, Revealing the origin of anisotropic rashba spin–orbital splitting and four-phonon scattering in strontium–tin–selenium thermoelectrics, *Adv. Funct. Mater.*, 2025, **35**, 2414288.
15 D. Liu, B. Qin and L. D. Zhao, SnSe/SnS: multifunctions beyond thermoelectricity, *Mater. Lab.*, 2022, **1**, 220006.
16 X. Wu, J. Huang and Z. Zhou, *et al.*, Mg_3Sb_2-based thermoelectrics: materials, interfaces, and devices, *Mater. Lab.*, 2023, **2**, 230003.
17 Y. Pei, C. Chang and Z. Wang, *et al.*, Multiple converged conduction bands in $K_2Bi_8Se_{13}$: a promising thermoelectric material with extremely low thermal conductivity, *J. Am. Chem. Soc.*, 2016, **138**, 16364–16371.
18 W. Li, S. Lin and M. Weiss, *et al.*, Crystal structure induced ultralow lattice thermal conductivity in thermoelectric Ag_9AlSe_6, *Adv. Energy Mater.*, 2018, **8**, 1800030.
19 F. Yu, X. Meng and J. Cheng, *et al.*, Novel n-type thermoelectric material of $ZnIn_2Se_4$, *J. Alloys Compd.*, 2019, **797**, 940–944.
20 S. Bai, X. Zhang and L. D. Zhao, Rethinking SnSe thermoelectrics from computational materials science, *Acc. Chem. Res.*, 2023, **56**, 3065–3075.
21 S. Bai, M. Wu and J. Zhang, *et al.*, Stacking pattern induced high ZTs in monolayer SnSSe and bilayer SnXY (X/Y = S, Se) materials with strong anharmonic phonon scattering, *Chem. Eng. J.*, 2023, **455**, 140832.
22 S. Tang, M. Wu and S. Bai, *et al.*, $SnSe_2$ monolayer with square lattice structure: a promising p-type thermoelectric material with an indirect bandgap and low lattice thermal conductivity, *J. Mater. Chem. C*, 2022, **10**, 16116–16125.
23 M. S. Toprak, C. Stiewe and D. Platzek, *et al.*, The impact of nanostructuring on the thermal conductivity of thermoelectric $CoSb_3$, *Adv. Funct. Mater.*, 2004, **14**, 1189–1196.
24 G. Romano, A. M. Kolpak and J. Carrete, *et al.*, Parameter-free model to estimate thermal conductivity in nanostructured materials, *Phys. Rev. B*, 2019, **100**, 045310.
25 S. Tang, S. Bai and M. Wu, *et al.*, Improving thermoelectric performance of asymmetrical Janus 1T-SnSSe monolayer by the synergistic effect of band convergence and crystal lattice softening under strain engineering, *Mater. Today Phys.*, 2022, **29**, 100923.
26 Y. Wu, B. Hou and C. Ma, *et al.*, Thermoelectric performance of 2D materials: the band-convergence strategy and strong intervalley scatterings, *Mater. Horiz.*, 2021, **8**, 1253–1263.
27 A. Hong, J. Gong and L. Li, *et al.*, Predicting high thermoelectric performance of ABX ternary compounds NaMgX (X = P, Sb, As) with weak electron-phonon coupling and strong bonding anharmonicity, *J. Mater. Chem. C*, 2016, **4**, 3281–3289.
28 A. M. El Maslout, J. P. Motte and C. Gleitzer, *et al.*, Preparation et proprietes d'un nouveau compose dans la serie LiMP: Le phosphure de lithium-cadmium LiCdP, *C. R. Seances Acad. Sci., Ser. C*, 1971, **273**, 707–710.
29 C. Tiburtius and H. U. Schuster, LiBeSb and LiZnBi, ternary compounds with a wurtzite-type lattice, *Z. Naturforsch.*, 1978, **33**, 35–38.
30 C. Tiburtius and H. U. Schuster, NaBeAs (Sb)-Ternäre Phasen im ''aufgefüllten'' NiAs (Ni_2In)-Typ/NaBeAs (Sb)-Ternary Phases in a ''Filled'' NiAs (Ni_2In)-Structure, *Z. Naturforsch. B*, 1977, **32**, 1133–1138.
31 B. Krenkel and H. U. Schuster, NaMgAs (Sb)-ternäre verbindungen mit modifizierter Cu_2Sb-Struktur/NaMgAs (Sb)-ternary compounds in a modified Cu_2Sb structure, *Z. Naturforsch. B*, 1978, **33**, 1080–1082.
32 Y. Benazouzi, H. Rozale and M. A. Boukli Hacene, *et al.*, Electronic and thermoelectric properties in Li-based Half–Heusler compounds: A first principle study, *An. West Univ. Timis., Phys. Ser.*, 2019, **61**, 44–55.
33 H. Al Salmah and S. Mehmood, Enhancement in the optoelectronic and thermoelectric properties of the NaASb (A = Ca, Sr and Ba) sodium antimonides via switching from *P*4/*nmm* to *P*62*m* symmetry, *J. Sci.: Adv. Mater. Devices*, 2024, **9**, 100662.
34 A. She, Y. Zhao and J. Ni, *et al.*, Investigation on transport properties and anomalously heat-carrying optical phonons in KXY (X= Ca, Mg; Y= Sb, Bi), *Int. J. Heat Mass Transfer*, 2023, **209**, 124132.
35 A. M. Ochs, G. H. Fecher and B. He, *et al.*, Synergizing a large ordinary Nernst effect and axis-dependent conduction polarity in flat band KMgBi Crystals, *Adv. Mater.*, 2024, **36**, 2308151.
36 A. She, Y. Zhao and J. Ni, *et al.*, Thermoelectric performance of Zintl compound KMgBi with layered structure, *J. Phys. Chem. Solids*, 2023, **178**, 111308.
37 V. Chaudhary, T. Maitra and T. Nautiyal, *et al.*, Effect of hydrostatic pressure and alloying on thermoelectric properties of van der Waals solid KMgSb: An ab initio study, *Phys. Rev. Mater.*, 2023, **7**, 095401.

38 D. Behera and S. K. Mukherjee, Insight to the structural, electronic, optical, and thermoelectric properties of NaCaSb and KCaSb Half Heusler compounds: a DFT approach, *JETP Lett.*, 2023, **117**, 687–700.
39 X. Zhang, L. Yu and A. Zakutayev, *et al.*, Sorting stable versus unstable hypothetical compounds: the case of multi-functional ABX Half–Heusler filled tetrahedral structures, *Adv. Funct. Mater.*, 2012, **22**, 1425–1435.
40 P. K. Kamlesh, R. Agarwal and U. Rani, *et al.*, First-principles calculations of inherent properties of Rb based state-of-the-art Half–Heusler compounds: promising materials for renewable energy applications, *Phys. Scr.*, 2021, **96**, 115802.
41 R. H. Cardoso Gil, N. Caroca-Canales and W. Hönle, *et al.*, Crystal structures of rubidium calcium arsenide, RbCaAs and of rubidium calcium antimonide, RbCaSb, *Z. Kristallogr. – New Cryst. Struct.*, 1998, **213**, 483–484.
42 X. Song, Y. Zhao and J. Ni, *et al.*, Thermal transport properties of anisotropic materials RbCaX (X = As, Sb) with strong anharmonicity, *Comput. Mater. Sci.*, 2022, **213**, 111618.
43 J. Hafner, *Ab initio* simulations of materials using VASP: Density-functional theory and beyond, *J. Comput. Chem.*, 2008, **29**, 2044–2078.
44 P. E. Blöchl, Projector augmented-wave method, *Phys. Rev. B: Condens. Matter Mater. Phys.*, 1994, **50**, 17953.
45 G. Kresse and D. Joubert, From ultrasoft pseudopotentials to the projector augmented-wave method, *Phys. Rev. B: Condens. Matter Mater. Phys.*, 1999, **59**, 1758.
46 J. P. Perdew, K. Burke and M. Ernzerhof, Generalized gradient approximation made simple, *Phys. Rev. Lett.*, 1996, **77**, 3865.
47 A. J. Cohen, P. Mori-Sánchez and W. Yang, Fractional charge perspective on the band gap in density-functional theory, *Phys. Rev. B: Condens. Matter Mater. Phys.*, 2008, **77**, 115123.
48 J. M. Crowley, J. Tahir-Kheli and W. A. Goddard III, Resolution of the band gap prediction problem for materials design, *J. Phys. Chem. Lett.*, 2016, **7**, 1198–1203.
49 J. Heyd, G. E. Scuseria and M. Ernzerhof, Hybrid functionals based on a screened Coulomb potential, *J. Chem. Phys.*, 2003, **118**, 8207–8215.
50 A. V. Krukau, O. A. Vydrov and A. F. Izmaylov, *et al.*, Influence of the exchange screening parameter on the performance of screened hybrid functionals, *J. Chem. Phys.*, 2006, **125**, 224106.
51 S. Grimme, S. Ehrlich and L. Goerigk, Effect of the damping function in dispersion corrected density functional theory, *J. Comput. Chem.*, 2011, **32**, 1456–1465.
52 S. Grimme, J. Antony and S. Ehrlich, *et al.*, A consistent and accurate ab initio parametrization of density functional dispersion correction (DFT-D) for the 94 elements H-Pu, *J. Chem. Phys.*, 2010, **132**, 154104.
53 A. Jain, S. P. Ong and G. Hautier, *et al.*, Commentary: the Materials Project: A materials genome approach to accelerating materials innovation, *APL Mater.*, 2013, **1**, 011002.
54 A. M. Ganose, J. Park and A. Faghaninia, *et al.*, Efficient calculation of carrier scattering rates from first principles, *Nat. Commun.*, 2021, **12**, 2222.
55 K. B. Spooner, A. M. Ganose and W. W. Leung, *et al.*, $BaBi_2O_6$: a promising n-type thermoelectric oxide with the $PbSb_2O_6$ crystal structure, *Chem. Mater.*, 2021, **33**, 7441–7456.
56 B. Monserrat, Electron-phonon coupling from finite differences, *J. Phys.: Condens. Matter*, 2018, **30**, 083001.
57 A. Togo and I. Tanaka, First principles phonon calculations in materials science, *Scr. Mater.*, 2015, **108**, 1–5.
58 E. V. Podryabinkin, E. V. Tikhonov and A. V. Shapeev, *et al.*, Accelerating crystal structure prediction by machine-learning interatomic potentials with active learning, *Phys. Rev. B*, 2019, **99**, 064114.
59 I. S. Novikov, K. Gubaev and E. V. Podryabinkin, *et al.*, The MLIP package: moment tensor potentials with MPI and active learning, *Mach. Learn: Sci. Technol.*, 2020, **2**, 025002.
60 M. E. Tuckerman, P. J. Ungar and T. Von Rosenvinge, *et al.*, *Ab initio* molecular dynamics simulations, *J. Phys. Chem.*, 1996, **100**, 12878–12887.
61 B. Mortazavi, E. V. Podryabinkin and I. S. Novikov, *et al.*, Accelerating first-principles estimation of thermal conductivity by machine-learning interatomic potentials: A MTP/ShengBTE solution, *Comput. Phys. Commun.*, 2021, **258**, 107583.
62 W. Li, J. Carrete and N. A. Katcho, *et al.*, ShengBTE: A solver of the Boltzmann transport equation for phonons, *Comput. Phys. Commun.*, 2014, **185**, 1747–1758.
63 W. Pearson, The Cu_2Sb and related structures, *Z. Kristallogr. – Cryst. Mater.*, 1985, **171**, 23–40.
64 L. Linowsky and W. Bronger, Synthese und Kristallstruktur von KMnP und KMnAs, *J. Inorg. Gen. Chem.*, 1974, **409**, 221–227.
65 J. Qiao, X. Kong and Z. X. Hu, *et al.*, High-mobility transport anisotropy and linear dichroism in few-layer black phosphorus, *Nat. Commun.*, 2014, **5**, 4475.
66 Y. Zhao, J. Qiao and P. Yu, *et al.*, Extraordinarily strong interlayer interaction in 2D layered PtS_2, *Adv. Mater.*, 2016, **28**, 2399–2407.
67 Y. Zhao, J. Qiao and Z. Yu, *et al.*, High-electron-mobility and air-stable 2D layered $PtSe_2$ FETs, *Adv. Mater.*, 2017, **29**, 1604230.
68 R. G. Pearson, Chemical hardness and bond dissociation energies, *J. Am. Chem. Soc.*, 1988, **110**, 7684–7690.
69 W. F. Perger, J. Criswell and B. Civalleri, *et al.*, Ab-initio calculation of elastic constants of crystalline systems with the CRYSTAL code, *Comput. Phys. Commun.*, 2009, **180**, 1753–1759.
70 Z. Wu, E. Zhao and H. Xiang, *et al.*, Crystal structures and elastic properties of superhard IrN_2 and IrN_3 from first principles, *Phys. Rev. B: Condens. Matter Mater. Phys.*, 2007, **76**, 054115.
71 N. Wang, C. Shen and Z. Sun, *et al.*, Thermal transport and mechanical properties of layered oxychalcogenides LaCuOX (X= S, Se, and Te), *ACS Appl. Energy Mater.*, 2022, **5**, 6943–6951.
72 S. Bai, J. Zhang and M. Wu, *et al.*, Theoretical prediction of thermoelectric performance for layered LaAgOX (X= S, Se) materials in consideration of the four-phonon and multiple carrier scattering processes, *Small Methods*, 2023, **7**, 2201368.

73 W. Voigt, Wechselbeziehungen zwischen zwei Tensortripeln.(Elastizität und innere Reibung.), in *Lehrbuch der Kristallphysik*, ed. W. Voigt, Springer, Berlin, 1966, pp. 560–800.
74 A. Reuß, Berechnung der fließgrenze von mischkristallen auf grund der plastizitätsbedingung für einkristalle, *J. Appl. Math. Mech.*, 1929, **9**, 49–58.
75 R. Hill, The elastic behaviour of a crystalline aggregate, *Proc. Phys. Soc., London, Sect. A*, 1952, **65**, 349.
76 S. F. Pugh, XCII. Relations between the elastic moduli and the plastic properties of polycrystalline pure metals, *Philos. Mag.*, 1954, **45**, 823–843.
77 N. Wang, M. Li and H. Xiao, *et al.*, Band degeneracy enhanced thermoelectric performance in layered oxyselenides by first-principles calculations, *npj Comput. Mater.*, 2021, **7**, 18.
78 J. Yuan, Y. Cai and L. Shen, *et al.*, One-dimensional thermoelectrics induced by Rashba spin-orbit coupling in two-dimensional BiSb monolayer, *Nano Energy*, 2018, **52**, 163–170.
79 F. Q. Wang, S. Zhang and J. Yu, *et al.*, Thermoelectric properties of single-layered SnSe sheet, *Nanoscale*, 2015, **7**, 15962–15970.
80 S. Foster and N. Neophytou, Effectiveness of nanoinclusions for reducing bipolar effects in thermoelectric materials, *Comput. Mater. Sci.*, 2019, **164**, 91–98.
81 S. Zhan, T. Hong and B. Qin, *et al.*, Realizing high-ranged thermoelectric performance in $PbSnS_2$ crystals, *Nat. Commun.*, 2022, **13**, 5937.
82 G. J. Snyder and E. S. Toberer, Complex thermoelectric materials, *Nat. Mater.*, 2008, **7**, 105–114.
83 G. Li, G. Ding and G. Gao, Thermoelectric properties of $SnSe_2$ monolayer, *J. Phys.: Condens. Matter*, 2016, **29**, 015001.
84 J. M. Skelton, L. A. Burton and S. C. Parker, *et al.*, Anharmonicity in the high-temperature *Cmcm* phase of SnSe: soft modes and three-phonon interactions, *Phys. Rev. Lett.*, 2016, **117**, 075502.
85 I. Mertig, R. Zeller and P. H. Dederichs, Ab initio calculations of the deviations from Matthiessen's rule for dilute ternary alloys, *Phys. Rev. B: Condens. Matter Mater. Phys.*, 1994, **49**, 11767.
86 H. Shao, X. Tan and G. Q. Liu, *et al.*, A first-principles study on the phonon transport in layered BiCuOSe, *Sci. Rep.*, 2016, **6**, 21035.
87 Y. Xiao, C. Chang and Y. Pei, *et al.*, Origin of low thermal conductivity in SnSe, *Phys. Rev. B*, 2016, **94**, 125203.
88 D. Aketo, T. Shiga and J. Shiomi, Scaling laws of cumulative thermal conductivity for short and long phonon mean free paths, *Appl. Phys. Lett.*, 2014, **105**, 131901.

